Journal of Zhejiang University-SCIENCE A (Applied Physics & Engineering) 2023 24(7):612-624
www.jzus.zju.edu.cn; www.springer.com/journal/11582
E-mail: jzus_a@zju.edu.cn

Research Article
https://doi.org/10.1631/jzus.A2200447

Square cavity flow driven by two mutually facing sliding walls

Bo AN[1,2,3], Josep M. BERGADÀ[4], Weimin SANG[1]✉, Dong LI[1], F. MELLIBOVSKY[5]

[1]*School of Aeronautics, Northwestern Polytechnical University, Xi'an 710072, China*
[2]*National Key Laboratory of Science and Technology on Aerodynamic Design and Research, Xi'an 710072, China*
[3]*Key Laboratory of Icing and Anti/De-icing, China Aerodynamics Research and Development Center, Mianyang 621000, China*
[4]*Department of Fluid Mechanics, Universitat Politécnica de Catalunya, Barcelona 08034, Spain*
[5]*Department of Physics, Aerospace Engineering Division, Universitat Politécnica de Catalunya, Barcelona 08034, Spain*

Abstract: We investigate the flow inside a 2D square cavity driven by the motion of two mutually facing walls independently sliding at different speeds. The exploration, which employs the lattice Boltzmann method (LBM), extends on previous studies that had the two lids moving with the exact same speed in opposite directions. Unlike there, here the flow is governed by two Reynolds numbers (Re_T, Re_B) associated to the velocities of the two moving walls. For convenience, we define a bulk Reynolds number Re and quantify the driving velocity asymmetry by a parameter α. Parameter α has been defined in the range $\alpha\in[-\pi/4, 0]$ and a systematic sweep in Reynolds numbers has been undertaken to unfold the transitional dynamics path of the two-sided wall-driven cavity flow. In particular, the critical Reynolds numbers for Hopf and Neimark-Sacker bifurcations have been determined as a function of α. The eventual advent of chaotic dynamics and the symmetry properties of the intervening solutions are also analyzed and discussed. The study unfolds for the first time the full bifurcation scenario as a function of the two Reynolds numbers, and reveals the different flow topologies found along the transitional path.

Key words: Two-sided wall-driven cavity; Velocity ratios; Transitions; Flow topology; Energy cascade

1 Introduction

A systematic research on the transitional dynamics of several 2D wall-driven cavity flows was performed in several previous studies (An et al., 2019, 2020a, 2020b). In particular, we took into consideration the flow within a square enclosure driven by the tangential motion of two opposing walls, with equal speed, in parallel and anti-parallel directions. As the driving velocity of the top and bottom walls had always the same magnitude, the problem was either reflection-symmetric with respect to the horizontal plane, or possessed a triad of symmetries including reflection with respect to any of the two diagonals and π-rotational invariance. In both cases, the reflection symmetries involved were shown to break at the first Hopf bifurcation.

For the classic lid-driven cavity flow (α=0), the appearance of the Hopf bifurcation was found at Reynolds number Re_α^H=8025±25 (An et al., 2020b), which was in good agreement with benchmark literature results, with estimations for the advent of time dependence at Reynolds numbers 8108.2±0.6 (Auteri et al., 2002), 8026.7 (Boppana and Gajjar, 2010), 8025.9 (Kalita and Gogoi, 2016), and 8051.0 (Nuriev et al., 2016). Non et al. (2006) investigated the first bifurcation in a spanwise extended square cavity, and they found out that the Hopf bifurcation occurred at a much lower Re_α^H=1040 for λ=11, with λ the wave number.

Square cavity flows driven by two or more walls have been considered in the literature to some extent. Perumal and Dass (2011) employed the lattice Boltzmann method (LBM) to prove the multiplicity of stable steady solutions that arise when two adjacent walls move away from their connecting corner at equal speeds. The new coexisting solutions broke the reflection symmetry about the diagonal. Something similar,

---

✉ Weimin SANG, aeroicing@sina.cn
Bo AN, https://orcid.org/0000-0001-8738-2504
Josep M. BERGADÀ, https://orcid.org/0000-0003-1787-7960
F. MELLIBOVSKY, https://orcid.org/0000-0003-0497-9052

Received Sept. 23, 2022; Revision accepted Jan. 5, 2023;
Crosschecked May 22, 2023

this time breaking the symmetry with respect to the two diagonals and keeping the invariance to π-rotation, was shown to happen for square cavities with four moving walls, when all pairs of adjacent walls either converged or diverged at the same rate. Prasad and Dass (2016) unveiled, using a high-order compact scheme, multiplicity of steady solutions also for the case of two facing walls moving in anti-parallel fashion. Symmetry-breaking pitchfork bifurcations Re_{α}^{P} were detected at $Re_{\alpha}^{\mathrm{P}}=983.5$ and 3203.0. For the parallel sliding wall case, Lemée et al. (2015) found a similar result for the pitchfork bifurcation, but they extended the analysis to higher values of the Reynolds number and detected a Hopf bifurcation of the asymmetric state at $Re_{\alpha}^{\mathrm{H}}=10750\pm250$. For the anti-parallel case and using an upwind compact difference scheme applied to the stream function formulation, Yu and Tian (2018) detected the steady state multiplicity and the pitchfork bifurcation at about the same value of the Reynolds number $Re_{\alpha}^{\mathrm{P}}=3200$. Yang and Zhang (2012) set the focus on the capability of the conservation-element-solution-element (CE/SE) method for resolving both corner and off-corner vortices at low Reynolds numbers, and they evaluated the flow inside the two-sided cavity with anti-parallel motion of the top and bottom walls.

All the aforementioned research on square cavities with two or four moving walls prescribed the same speed to them all. As a result, the flow presented symmetries and could only be evaluated as the sole function of one parameter, the Reynolds number *Re*. The results obtained for the symmetric problems set the stage for tackling more complex flow dynamics scenarios by taking into consideration a second parameter to introduce an asymmetry through applying different velocities to each one of the moving walls. Hammami et al. (2018) made a first step in this direction by studying the flow in rectangular cavities of varying aspect ratio $0.25\leqslant A\leqslant 1.00$ ($A=H/L$, H is the height of a square cavity, and L is the bottom side of a square cavity) driven by the independent motion of two-sided wall-driven cavity flow with various values of the velocity ratio $0.250\leqslant\beta\leqslant 0.825$ ($\beta=V/U$, U is the driving velocity on the lid and V is the driving velocity along the vertical side). Their focus was placed on the bifurcation phenomena and, in particular, on the first Hopf bifurcation. Shankar and Deshpande (2000) presented an overview on the fluid mechanics in the lid-driven cavity for 2D and 3D geometries with different aspect ratios through experiments and numerical simulations, in which, the corner eddies, longitudinal vortices, non-uniqueness, transitions, and turbulences were discussed in detail. Albensoeder et al. (2000), Albensoeder and Kuhlmann (2002), and Romanò et al. (2017, 2020) did a tremendous work on the two-sided lid-driven cavity flow for both parallel and anti-parallel wall motions. Both 2D and 3D geometries were considered for research on the linear stability, flow topology, and Lagrangian chaos. Speaking of the Lagrangian chaos, some studies (Franjione et al., 1989; Iwatsu et al., 1989; Leong and Ottino, 1989) should be mentioned as well, which are different from the present study, where the Eulerian chaos is concerned.

Despite the considerable amount of work done on the classic lid-driven cavity flow, little effort has been devoted to understanding the flow dynamics inside a 2D square cavity driven by the parallel motion of two mutually facing walls with different velocities. This difference in driving conditions has a subtle impact on the transitions, which has been inspired by previous research. To the best of our knowledge, the transition mechanisms underlying slight disruption of the problem symmetries have not been addressed. Our results are, in this sense, novel, and may help understand the effects of imperfect symmetries in this and many other problems. Here we undertake a thorough systematic analysis of this problem, with special attention in regards to the first Hopf and Neimark-Sacker bifurcations, the onset of chaos, the symmetry disruption, and the energy cascade, which serve to link the different vortical structures that appear in the flow to their corresponding frequency peaks and associated energy. Since the present study is an extension of authors' previous work, the in-house code validation and the resolution study will not be repeated in the present manuscript, but can be found in our previous work (An et al., 2019, 2020a, 2020b).

The outline of the paper is as follows. In Section 2, we address the mathematical formulation and numerical methods used. Results are presented in Section 3, alongside with a discussion. Finally, we summarize the main findings in Section 4, where the impact of the second parameter, the top-to-bottom velocity ratio, on the flow transitions is addressed in detail. The flow field evolution is analyzed and discussed as well. Concluding remarks are also given in Section 4.

2 Mathematical modelling and numerical approach

Considering the flow of an incompressible Newtonian fluid of kinematic viscosity ν inside a square cavity of side L, driven by the independent sliding of the top and bottom walls at constant speeds U_T and U_B, respectively (Fig. 1a), the Reynolds numbers defined for the top and bottom lids Re_T and Re_B take the form:

$$Re_\mathrm{T}=\frac{U_\mathrm{T}L}{\nu},\quad Re_\mathrm{B}=\frac{U_\mathrm{B}L}{\nu}. \tag{1}$$

In order to make the symmetry disruptions explicit, it is more convenient to describe the motion of combined top and bottom lids using an alternative set of parameters:

$$Re=\frac{UL}{\nu}=\sqrt{Re_\mathrm{T}^2+Re_\mathrm{B}^2},\quad \alpha=\mathrm{arctan2}(Re_\mathrm{B},\,Re_\mathrm{T}), \tag{2}$$

which is equivalent to exploring the 2D Cartesian parameter space $(Re_\mathrm{T},\,Re_\mathrm{B})$ in polar coordinates $(Re,\,\alpha)$ (Fig. 1b). The unique velocity that goes into the bulk Reynolds number Re is related to the top and bottom velocities as $U_\mathrm{T}=U\cos\alpha$ and $U_\mathrm{B}=U\sin\alpha$.

The dynamics of a Newtonian fluid is governed by the Navier-Stokes equations, which, after non-dimensionalisation with length and time scales L and L/U, read as

$$\frac{\partial \boldsymbol{u}}{\partial t}+(\boldsymbol{u}\cdot\nabla)\boldsymbol{u}=-\nabla p+\frac{1}{Re}\nabla^2\boldsymbol{u},\quad \nabla\cdot\boldsymbol{u}=0, \tag{3}$$

with unknowns $\boldsymbol{u}(\boldsymbol{r},\,t)=(u,\,v)$ and $p(\boldsymbol{r},\,t)$, the non-dimensional velocity and pressure fields, respectively, at non-dimensional space coordinates $\boldsymbol{r}=(x,\,y)$, $x\in[-0.5,\,0.5]$, $y\in[-0.5,\,0.5]$, and advective time $t\geqslant 0$. The coordinate origin has been set for convenience at the centre of the cavity. The boundary conditions for velocity are non-slip homogeneous for the left and right walls $[\boldsymbol{u}(\pm0.5,\,y,\,t)=(0,\,0)]$ and prescribed constant velocity for the top $[\boldsymbol{u}(x,\,0.5,\,t)=(\cos\alpha,\,0)]$ and for the bottom $[\boldsymbol{u}(x,\,-0.5,\,t)=(\sin\alpha,\,0)]$ walls. Homogeneous Neumann boundary conditions for pressure are applied on all walls.

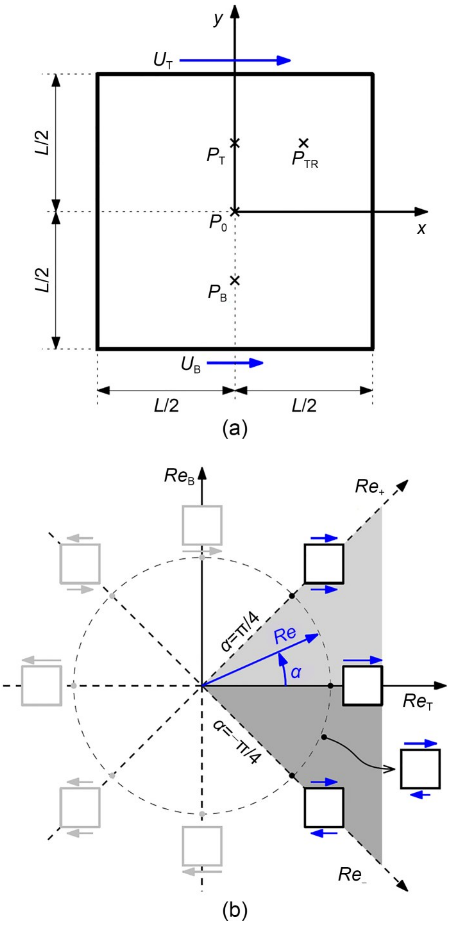

(a)

(b)

Fig. 1 Two-facing-wall-driven square flow: (a) domain; (b) parameter space

The two-opposing-wall-driven square cavity flow problem is invariant under some sort of symmetry operations (Eq. (S1) in the electronic supplementary materials (ESM)) and can be expressed in terms of the pair $(Re,\,\alpha)$. The symmetries read as

$$\begin{aligned}
&M_y\Big|[u,\,v,\,p](x,\,y,\,t;\,Re,\,\alpha)=[-u,\,v,\,p](-x,\,y,\,t;\,Re,\,\pi+\alpha),\\
&M_x\Big|[u,\,v,\,p](x,\,y,\,t;\,Re,\,\alpha)=[u,\,-v,\,p]\left(x,\,-y,\,t;\,Re,\,\frac{\pi}{2}-\alpha\right),\\
&\Re_\pi\Big|[u,\,v,\,p](x,\,y,\,t;\,Re,\,\alpha)=[-u,\,-v,\,p]\left(-x,\,-y,\,t;\,Re,\,-\frac{\pi}{2}-\alpha\right),
\end{aligned} \tag{4}$$

where M_x and M_y are the mirror symmetries with respect to the horizontal and vertical mid-planes, respectively, and $\mathfrak{R}_\pi$ is the π-rotational symmetry.

As a consequence, only the range $\alpha\in[-\pi/4,\pi/4]$ needs to be explored, as any value of α can be mapped onto the right-angle sector by the appropriate application of a suitable combination of any two of the three symmetries. In other words, any case ($Re_{\rm T}$, $Re_{\rm B}$) has an equivalent with $Re_{\rm T}\geqslant|Re_{\rm B}|$, implying $-Re_{\rm T}\leqslant Re_{\rm B}\leqslant Re_{\rm T}$, or $Re_+\equiv Re_{\rm T}+Re_{\rm B}\geqslant 0$ and $Re_-\equiv Re_{\rm T}-Re_{\rm B}\geqslant 0$. There are several ways to achieve this. For instance, Re_+ might be forced to be positive by application, if required, of M_y, which restricts parameter space to the half plane $\alpha\in[-\pi/4, 3\pi/4]$. Then, if not already so, the resulting Re_- might also be brought to be positive by application of M_x, further restricting parameter space to just the quadrant $\alpha\in[-\pi/4, \pi/4]$ (shaded region in Fig. 1b). After due mapping, $\alpha=0$ represents the classic lid-driven square cavity flow, while $\alpha=\pm\pi/4$ corresponds to the two-facing-wall-driven square cavity flows with both walls moving at the same speed in the same ($\pi/4$) and opposite ($-\pi/4$) directions. Notice however that the Reynolds number in the previous symmetric cases, as discussed in the literature, is usually defined as $\hat{Re}=\hat{U}L/\nu$, with $\hat{U}\equiv|U_{\rm T}|=|U_{\rm B}|$. Comparison of results requires an appropriate correction to the advective time scale $t_{\rm c}=\sqrt{2}\,\hat{t}_{\rm c}$ and Reynolds number $Re=\sqrt{2}\hat{Re}$. In the present study, we will focus on the case with the two walls moving in opposite directions, which corresponds to the octant $\alpha\in[-\pi/4, 0]$ (dark grey region shown in Fig. 1b).

We choose to solve the 2D equations of motion inside the cavity with the 9-bit D2Q9 lattice Boltzmann model presented by Qian et al. (1992) and the non-equilibrium extrapolation scheme proposed by Guo et al. (2002), which provides second-order accuracy in both space and time. The numerical method has been coded in-house and extensively tested in the past (An et al., 2019, 2020a, 2020b), where thorough mesh-independence studies were undertaken. Based on the previous experience and comprehensive mesh convergence analysis, the square cavity has been resolved with a uniform Cartesian mesh of $N_x\times N_y=1024\times1024$ grid points in the horizontal and vertical directions, respectively.

For the sake of simplicity, simulations have been carried out with a top wall velocity $U_{\rm T}=0.1$, and as a result, the associated Mach number is given as $M=\sqrt{3}\,U$ according to the LBM particulars. The bottom wall velocity has been made to vary in the range $U_{\rm B}\in[-0.4, 0.0]$. Cases with $|U_{\rm B}|>|U_{\rm T}|$ are redundant on account of the symmetries of the problem, but have been run all the same as a check for numerical compressibility effects associated to LBM. All runs have however been mapped onto the $\alpha\in[-\pi/4, \pi/4]$ quadrant using the symmetries as required and consistently non-dimensionalised to allow straightforward comparison. The bulk Reynolds number is prescribed through the adjustment of the relaxation time parameter τ via the relation $\nu=(1/6)(2\tau-1)(\Delta x)^2/\Delta t$, where $\Delta x\equiv L/N_x$ and $c=\Delta x/\Delta t$ is the particle velocity across the lattice. Four probes used to collect time series are planted inside the domain, and their coordinates are respectively given by $P_0=(0, 0)$, $P_{\rm B}=(0, -L/4)$, $P_{\rm T}=(0, L/4)$, and $P_{\rm TR}=(L/4, L/4)$.

Parameter space has been systematically explored by continuously increasing the bulk Reynolds number Re along nine straight lines along $\tan\alpha=-0.05$, -0.10, -0.25, -0.50, -0.75, -0.95, -1.00, -2.00, and -4.00. The cases $\tan\alpha=-2.0$ and -4.0 correspond to symmetry operations on the cases $\tan\alpha=-0.50$ and -0.25, respectively, but with higher associated Mach numbers ($M=-0.3464$ and $M=-0.6928$ respectively for $\tan\alpha=-2.0$ and -4.0), so that differences in the results can be fully ascribed to compressibility results and serve therefore as a further validation of the method.

The critical Hopf has been re-computed for the $\alpha=-0.2449$ and -0.4640 cases but with larger values of the dimensional velocities used in the LBM simulations (these were in fact the cases with $\tan\alpha=-2.0$ and -4.0). The maximum lid velocity was therefore increased from 0.1 to 0.4 and 0.2, respectively, evidently challenging the incompressibility limit. As point of fact, the case doubling the maximum dimensional lid velocity pushed the Hopf bifurcation slightly from $Re^{\rm H}=15930\pm60$ to 16070 ± 140 showing acceptably low compressibility effects. This was not so for the case multiplying the maximum velocity four-fold, which resulted in a considerable increase from $Re^{\rm H}=13450\pm50$ to 14220 ± 200. It is therefore obvious that the implementation of LBM used in this study is not appropriate when using lid velocities beyond 0.2. Keeping the lid velocity low, with its inconvenient impact on the time step, is mandatory. Or else, a variant of the LBM fulfilling incompressibility might also be used (Guo et al., 2000).

3 Results and discussion

The cases $\alpha=\pm\pi/4$ were thoroughly analyzed by An et al. (2020b), where the bifurcation path leading to the onset of chaotic dynamics was presented alongside a detailed inspection of the evolution of the flow topology and its symmetries. Notice that for this particular case, in which the top and bottom lids are moving in opposite directions with the same speed, the asymmetry shows up as the instability appears. Here we extend the study to intervening negative values of α in order to clarify the evolution from the cavity flow driven by two mutually facing walls sliding with equal but opposed velocities to the classic lid-driven cavity flow, represented by $\alpha=0$. The aim remains the same, namely the identification of the transition path that leads to chaotic dynamics and the characterization of the flow topology along the way. The computational cost of pinpointing the precise critical values of the parameters for each one of the bifurcations is unaffordable with only a time-stepping code. We choose instead to provide ranges for the transitions, which we express through a best estimate plus/minus a deviation. The best estimate is obtained by averaging the parameter values of the threshold solutions before and after each bifurcation while the maximum deviation results from the parameter step between the same two bordering solutions.

3.1 Hopf bifurcation

For $\alpha=-\pi/4$, the flow transition from steady to unsteady periodic arises as the top (and bottom) lid Reynolds numbers are increased simultaneously from 10100 to 10200 (An et al., 2020b). In terms of the bulk Reynolds number, the Hopf bifurcation occurs accordingly somewhere around $Re^{\mathrm{H}}=14390\pm25$. For $\alpha=0$ (the classic lid-driven square cavity flow), the Hopf bifurcation is known to be supercritical and to occur for $Re^{\mathrm{H}}=8025\pm25$ (Auteri et al., 2002; Boppana and Gajjar, 2010; Kalita and Gogoi, 2016; Nuriev et al., 2016; An et al., 2020b).

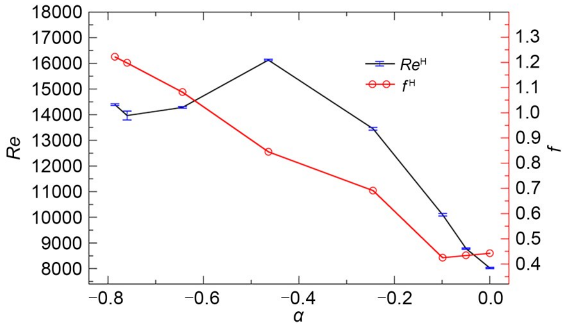

Fig. 2 Hopf bifurcation in Re-α parameter space. The critical Reynolds number for the Hopf bifurcation (Re^{H}) is shown as a function of α (black line, blue error bars denote uncertainty in its determination) along with the Hopf frequency (f^{H}), as approximated by the frequency of the first periodic solution after crossing the Hopf point. References to color refer to the online version of this figure

Fig. 2 shows the critical bulk Reynolds number for the Hopf bifurcation as a function of α. The bifurcation has been determined to within about 50 Reynolds number units. The bulk Reynolds number increases fast from the classic lid-driven square cavity flow case as the second (facing) wall is set into opposing motion. As a matter of fact, the Hopf bifurcation is postponed to $Re^{\mathrm{H}}=16130\pm30$, about double of the original value ($\alpha=0$), by the time $\alpha=-0.464$ is reached. But the stabilizing trend is thence reversed and the critical point for the onset of time-dependence is brought down to about $Re^{\mathrm{H}}=14390\pm25$ for $\alpha=-\pi/4$. There is a relative minimum when the value of $\alpha$is larger than or approximately equal to $-\pi/4$. Because of the symmetries of the problem, the case $\alpha=-\pi/4$ must act as a relative extremum, all properties having null slope as a function of α. Therefore, the bulk Reynolds number Re_{α}^{H} must either be a relative minimum or, apparently in this case, a relative maximum. The frequency f of the first periodic solution encountered upon increasing the bulk Reynolds number at a fixed α has been used as a harbinger of the Hopf frequency f^{H}. These are shown in Fig. 2. Starting from the classic lid-driven cavity flow $\alpha=0$, with $f=0.4425$ (Auteri et al., 2002; Boppana and Gajjar, 2010; Kalita and Gogoi, 2016; Nuriev et al., 2016; An et al., 2020b), the Hopf frequency f^{H} initially declines as α is reduced into negative values. The decrease is only mild and reaches $f=0.425$ for $\alpha=-0.099$ before bouncing back. From this point, the frequency rapidly increases to finally reach a maximum of about $f=1.222$ for $\alpha=-\pi/4$. It is realized as well, the 3D instabilities are supposed to occur far before $Re=10000$, if a cuboidal lid-driven cavity with square cross section is considered (Romanò et al., 2017, 2020).

Fig. 3 compares various steady state solutions for different α in the immediate vicinity of the Hopf bifurcation. As expected, there is a large central vortex flanked by three smaller vortices for $\alpha=0$ (Fig. 3a).

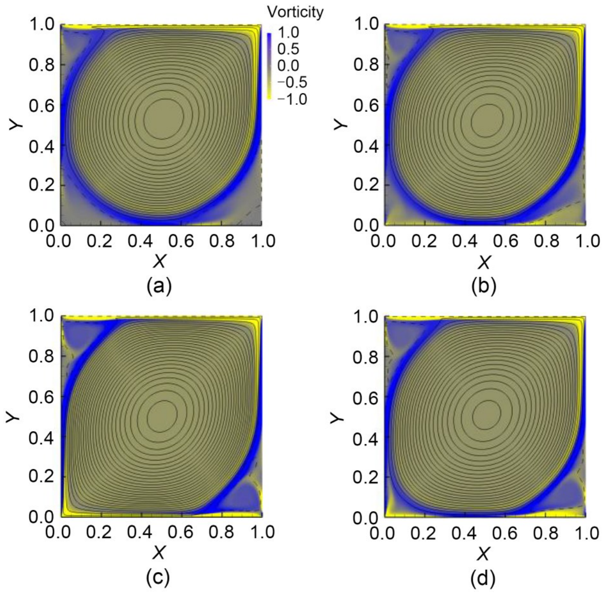

Fig. 3 Stream function isolines and vorticity color maps of steady solutions at Reynolds numbers just before the Hopf bifurcation. Vorticity ranges from −1.0 (yellow) to +1.0 (blue), as indicated by the color bar panel: (a) *Re*=8000, *α*=0; (b) *Re*=10050, *α*=−0.099; (c) *Re*=13400, *α*=−0.2499; (d) *Re*=14354, *α*=−π/4=−0.7854. References to color refer to the online version of this figure

Reducing α noticeably changes the bottom-right corner vortex (Fig. 3b). Further decreasing to α=−0.2449, the flow in this bottom right corner develops into a π-rotated weaker version of the vortical structure at the top-left corner, while the vortex in the bottom-left corner clearly weakens (Fig. 3c). Beyond this point, the π-rotational symmetry is gradually but steadily restored and then fully recovered when $\alpha=-\pi/4$ is reached (Fig. 3d).

Beyond the Hopf bifurcation the flow becomes periodic, as illustrated for $\alpha=-0.644$ at $Re=14313$ by the time signal, phase map, and spectrum of Fig. 4. The main panel depicts the Fourier transformation of the horizontal velocity u_x at point P_{TR}, and the time signal is shown in the top inset. The spectrum has a sharp peak at $f=1.082$ (associated period $T=1/f=0.9242$) and secondary (harmonic) peaks at integer multiples, as corresponds to a periodic signal. Fig. 4b shows the phase trajectory of a periodic solution, being a closed loop.

As previously stated, the following vortex color maps are sketched without showing the cavity axes for a better view of the flow topology details along the edge. For the classic single-lid-driven cavity (α=0, Fig. 5a), the time dependence shows mainly as a wave

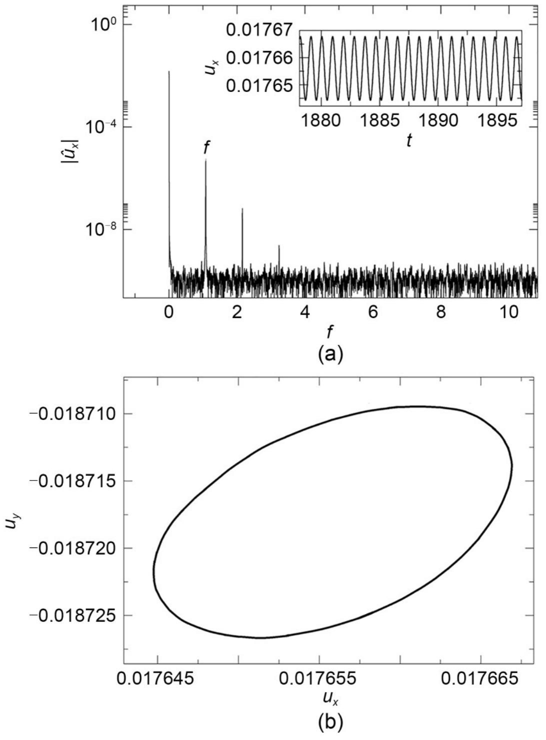

Fig. 4 Periodic solution for *α*=−0.644 at a bulk Reynolds number *Re*=14313: (a) spectral power density $|\hat{u}_x|$ of the horizontal velocity signal u_x as measured at probe P_{TR}; (b) phase-map projection on the u_x-u_y plane. u_y is the vertical velocity

train of vorticity knots that travels clockwise along the outward perimeter of the central core vortex. The top-left corner vortex shrinks and grows as the passage of the wave compresses and releases the space it occupies. This oscillation in size of the top-left corner is also largely perceptible for $\alpha=-0.099$ (Fig. 5b), but the wavy oscillation of the core vortex boundary is no longer as conspicuous. The situation remains fairly unaltered for $\alpha=-0.2499$ (Fig. 5c) as the new vortex at the bottom-right corner, which has grown discernible already for the steady solution, appears quite unaffected by the dynamics, possibly due to the lower local Reynolds number associated with the bottom lid. As the symmetry parameter increases towards $\alpha=-\pi/4$, the flow gradually evolves into a space-time symmetry consisting of invariance to evolution by half a period followed by π-rotation. This symmetry is evident at $\alpha=-\pi/4$ (Fig. 5d), where any two snapshots exactly $T/2$ apart are related by a π-rotation. For a better grasp of the time-dynamics, Videos S1–S5 at the same values of the driving parameters are provided in the ESM.

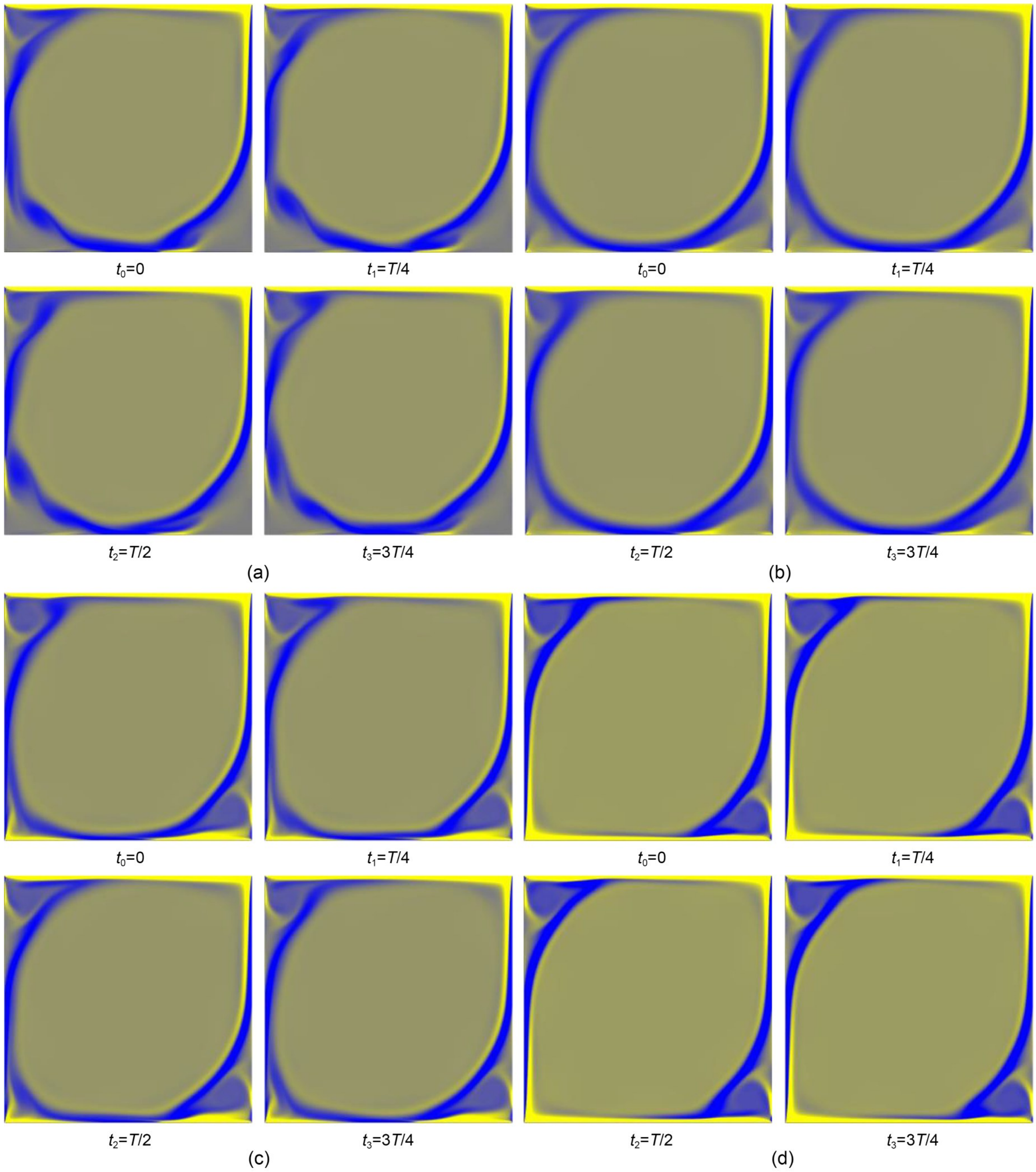

Fig. 5 Vorticity color maps of periodic solutions. Four snapshots are shown at instants 0, T/4, T/2, and 3T/4 equispaced along a full period T and the corresponding values of the parameters are: (a) Re=12000, α=0; (b) Re=10351, α=−0.099; (c) Re=14431, α=−0.2499; (d) Re=14496, α=−π/4. Cavity size and color coding as for Fig. 3 (Videos S2–S5 in the ESM)

3.2 Quasi-periodic and chaotic onset

A sufficient further increase of the bulk Reynolds number at a fixed α destabilizes the periodic solution and the flow evolves into quasi-periodicity. Taking the case ($\alpha=-0.644$) for illustration purposes, the flow is found to remain periodic up to Re=15438, well beyond the Hopf bifurcation, but it becomes quasi-periodic instead for Re>15625, which points at the advent of a Neimark-Sacker bifurcation. Beyond this bifurcation, the flow is observed to finally evolve into chaos, following a prototypical Ruelle & Takens scenario (Ruelle and Takens, 1971; Newhouse et al., 1978). Fig. 6a shows phase-map trajectories as well as the frequency spectrum at Re=15438 and 15625 for $\alpha=-0.644$. While the former closes in a loop every period, the latter possesses, beyond the fast dynamics that are evidently associated to the former solution, a second slower time-dynamics that makes the trajectory wind around a torus, filling it densely. At Re=15438, the spectrum in Fig. 6b confirms the periodic orbit hypothesis, with an associated non-dimensional frequency f_1=1.05. Notice that all other peaks are mere harmonics of the fundamental frequency. The sable periodic orbit is replaced, at Re=15625, by a quasi-periodic solution. The spectrum remains discrete but peaks arise at all linear combinations of the fundamental (ostensibly inherited from the periodic solution) f_1=1.049 and modulational f_2= 0.119 frequency peaks. The rotation number is f_1/f_2= 8.815, which explains why the phase-map trajectory almost closes every pseudo-periodic loops.

The modulational frequency peak is distinct though barely noticeable, but quasi-periodicity develops non-linearly as the bulk Reynolds number is further increased beyond the Neimark-Sacker bifurcation, which we pinpoint at $Re^{\mathrm{NS}}=15470\pm30$.

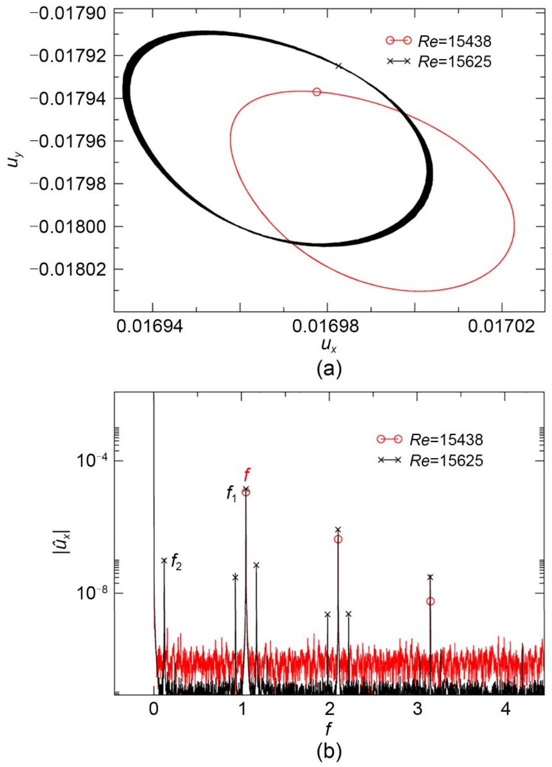

Fig. 6 Neimark-Sacker bifurcation for α=−0.644: (a) phase-map trajectories projected on the u_x-u_y plane as measured by probe P_{TR} of periodic (red, Re=15438) and quasi-periodic (black, Re=15625) solutions just before and after bifurcation; (b) spectrum of the horizontal velocity signal u_x from the same probe and for the same solutions α=−0.644. References to color refer to the online version of this figure

Moving to slightly larger values of Re>15750, Fig. 7b depicts the u_x spectrum across the transition from quasi-periodicity into chaos. The flow inside the cavity is undoubtedly quasi-periodic at Re=15750, but becomes gradually chaotic as the bulk Reynolds number is increased to 15875 and beyond. While, the spectrum still shows some remnants of the original frequencies f_1 and f_2, the fundamental peaks are now surrounded by broadband noise associated to chaotic dynamics Reynolds numbers.

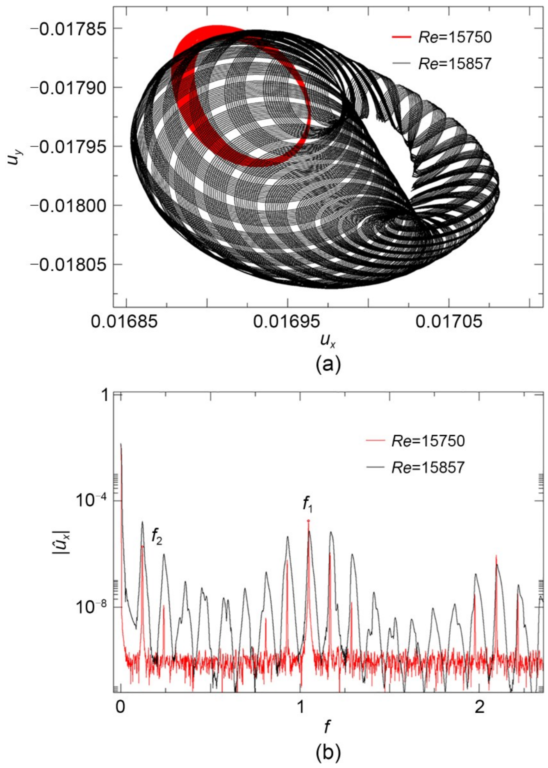

Fig. 7 Onset of chaotic dynamics for α=−0.644: (a) phase-map trajectories projected on the u_x-u_y plane as measured by probe P_{TR} of quasi-periodic (red, Re=15750) and time-chaotic (black, Re=15875) solutions just before and after the global bifurcation; (b) spectrum of the horizontal velocity signal u_x from the same probe and for the same solutions. References to color refer to the online version of this figure

The slow time-dynamics associated to quasi-periodicity is barely detectable in any representation of the flow fields, its effect merely consisting in a very slight modulation of the fast dynamics already described for the periodic solutions. A Poincaré section ($u_x=u_x^t$ and $\partial u_x/\partial t>0$) has been purposely defined in order to quotient out the fast dynamics associated to the Hopf frequency. Subsequently, the effects of the modulational frequency on the flow field can be illustrated through a collection of snapshots from these crossings. In particular, three consecutive crossings of the Poincaré section are sufficient for the solution to complete a full revolution on the torus surface, as required by the specific value the rotation number takes. The corresponding vorticity color maps are shown in Fig. 8. Videos S6–S10 are provided for various values of α in the ESM to show how the fast dynamics completely masks the manifestation of the slow dynamics.

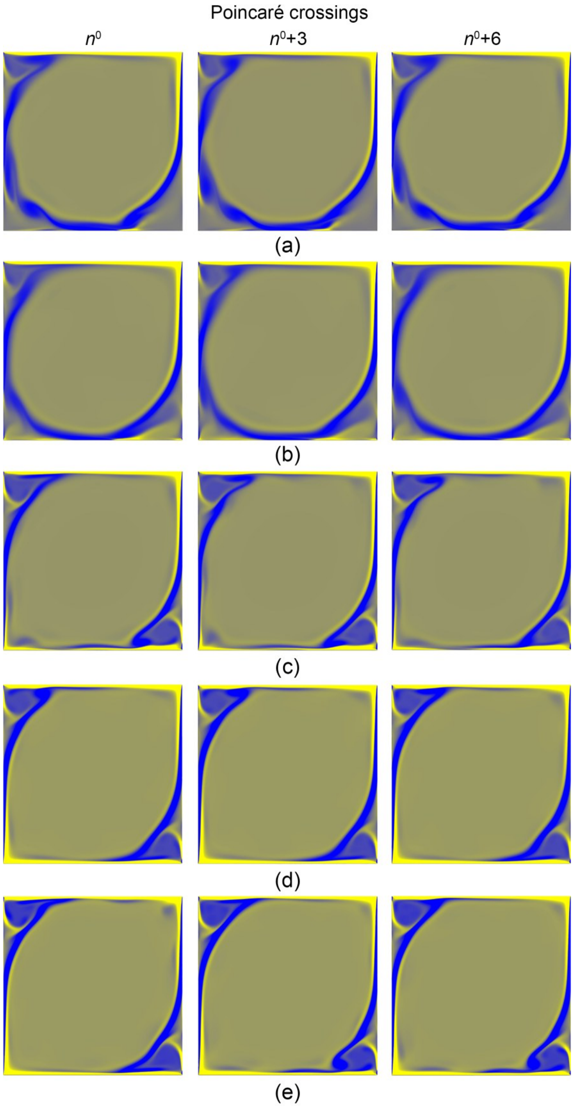

Fig. 8 Quasi-periodic solution for various values of α as illustrated by vorticity color maps of snapshots taken at three consecutive crossings (n^0 is the first crossing) of a Poincaré section defined by $u_x = u_x^{\prime}$ and $\partial u_x/\partial t>0$ as required by the rotation number for a full winding around the torus: (a) α=0, *Re*=14000; (b) α=−0.099, *Re*=11557; (c) α=−0.464, *Re*=17888; (d) α=−0.760, *Re*=15862; (e) α=−π/4, *Re*=19799. Cavity size and color coding as for Fig. 3 (Videos S6–S10 in the ESM)

The differences upon successive crossings evince the modulational dynamics of the quasi-periodic solutions emerged from the Neimark-Sacker bifurcation. Due to the proximity between the Neimark-Sacker and the onset of chaos, the cases $\alpha=-0.099$ (Fig. 8b) and −0.760 (Fig. 8d) barely show any indication of quasi-periodicity, although close inspection does indeed reveal some modulational dynamics (the related videos in the ESM). The stroboscopic effect is instead very prominent for the classic cavity (Fig. 8a), with the vorticity knots that circle the core vortex evidently pulsate at every consecutive crossing of the Poincaré section. The same effect is apparent on the top-left and bottom-right vortices for α=−0.464 (Fig. 8c) and sticks particularly out for the symmetric case $\alpha=-\pi/4$ (Fig. 8e), as the quasi-periodic solution has been able to evolve non-linearly far from its bifurcation point thanks to the strong resistance of the flow to the final destabilization into chaotic motion (Videos S11 and S12 in the ESM).

The Neimark-Sacker and chaotic-transition points have been extended into lines by carrying the analysis just illustrated to all other values of α considered. The dependences on α of the critical values associated to the Neimark-Sacker (Re^{NS}) and the global bifurcation (Re^{C}) that triggers chaotic dynamics are presented in Fig. 9, alongside those corresponding to the preceding Hopf bifurcation (Re^{H}). Both critical values start high for the classic lid-driven square cavity and drop sharply as the bottom wall is set in anti-parallel motion. Minimum

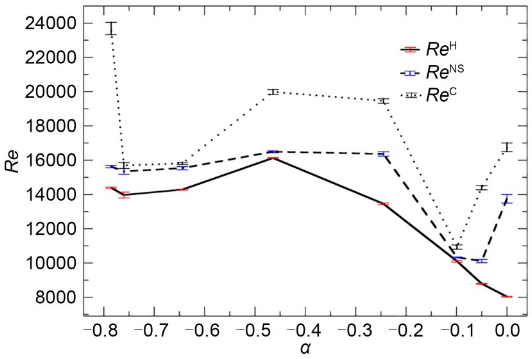

Fig. 9 Critical value for the Hopf (Re^{H}, solid line), Neimark-Sacker (Re^{NS}, dashed), and chaos-triggering (Re^{C}, dotted) bifurcations in *Re*-α parameter space. Error bars indicate the degrees of uncertainty in the determination of the critical lines

critical values Re^{NS}=10110±50 and Re^{C}=10930±130 are observed for α=−0.0499 and −0.0990, respectively. The trend is reversed at the minimum, and the critical values grow fast to reach a plateau around a maximum that, in our coarsely discretized parameter space, we identify at α=−0.499. The maximum is global for the Neimark-Sacker, with Re^{NS}=16490±50, but only local for the transition to chaos, with Re^{C}=20000±150. Reducing α beyond −0.0464 brings Re^{NS} slowly down to a new minimum Re^{NS}=15340±170 for α=−0.760, before bouncing towards a final maximum Re^{NS}=15630±70 at α=−π/4. Something similar happens for the onset of chaos, expect that the drop from the maximum at α=−0.499 is somewhat sharper, that the minimum at α=−0.760 is Re^{C}=15690±130, and the maximum for α=−π/4 is global at Re^{C}=23690±350. It therefore seems that a very slight asymmetry in the driving velocities destabilizes the flow into chaotic dynamics much more efficiently than the increase of the bulk Reynolds number.

Fig. 10 depicts the chaotic solution at Reynolds number Re=19375 and α=−0.644. The flow topology of the solution is illustrated by a single instantaneous snapshot of stream function isocontours and vorticity color map in Fig. 10a. The large central vortex still dominates the bulk of the flow and the overall flow topology is not very different from the steady solution at somewhat lower values of Re. The solution is temporally chaotic but not spatio-temporally chaotic, at least when assessed globally. The small eddies at the top-left and bottom-right corners, however, become decorrelated from one another, as comparison with the periodic solution at a different value of α (α=−π/4 and Re=14496, Fig. 5d), reveals. The vorticity color map underlines the regions where high shear is to be found. The interfaces between the main core vortex and the smaller corner vortices are responsible for the instability that introduces chaotic dynamics. The solution is temporally chaotic, as clear from the phase-map projections of Fig. 10b. Fig. 10c presents the spectrum of the u_x velocity signal (shown in the inset). Besides the broadband noise that pervades the full spectrum, the fundamental f_1 and modulational f_2 frequencies inherited from the quasi-periodic solution are still clearly recognizable, indicating that the solution retains a large degree of coherence.

In Fig. 11, the two relevant frequency peaks labelled as f_1 and f_2 are again observed in logarithmic scale. The frequency f_1, characterizes the higher energy level associated to the time dynamics of the main central vortex in Fig. 10a. The frequency f_2 represents instead the small-scale vortex interaction dynamics. Around this particular peak, several similar peaks also arise. We speculate that these peaks are characterizing the smaller vortical structures also appearing nearby the two vortices at the top-left and bottom-right corners. Notice that in the inertial subrange, the energy

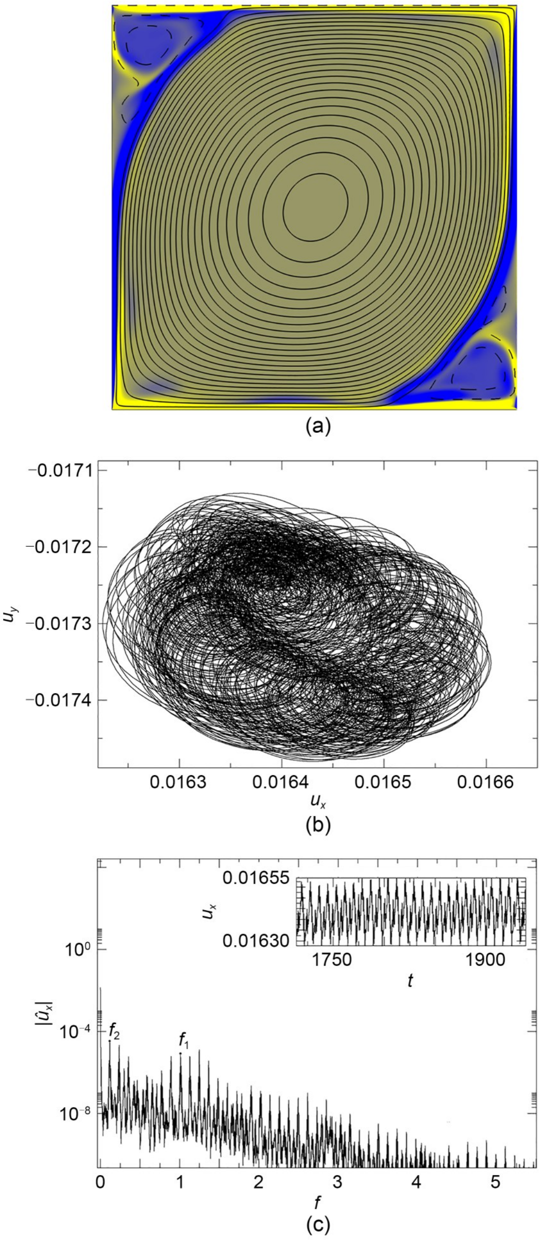

Fig. 10 Chaotic results at Re=19375, with α=−0.644: (a) stream function contours and vorticity color map (cavity size and color coding as for Fig. 3); (b) phase-map projection on the u_x-u_y plane; (c) spectrum $|\hat{u}_x|$ of time series u_x (inset)

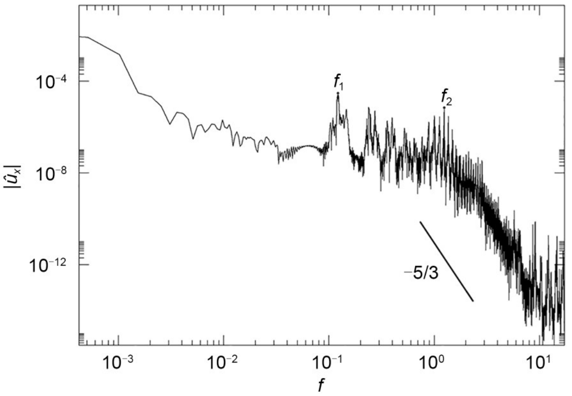

Fig. 11 Spectral decomposition of time series u_x at Re =19375, with α=−0.644

decays with a slope very close to −5/3, in good agreement with published data (Jiménez, 2012; Vassilicos, 2015; Alexakis and Biferale, 2018). Videos S11 and S12 show the flow dynamics of the α=−0.644, Re= 19375 and 23750 cases.

4 Conclusions

We have explored the effects of the independent sliding of two mutually facing driving walls on the flow within a square cavity. The two degrees of freedom associated with the two independent wall velocities have been parameterized using a bulk flow parameter, the bulk Reynolds number Re, and an asymmetry parameter α for the driving velocities. In this setting, α=0 represents the classic lid-driven cavity flow, whereas $\alpha=-\pi/4$ corresponds to the two facing walls moving in opposite directions at the same speed. All bifurcations, Hopf, Neimark-Sacker, and the onset of chaos, have been presented as a function of the parameter α, fully clarifying the transitional flow topology within two-sided square cavities.

We have found, as expected, that the first instability is always a Hopf bifurcation, such that the flow becomes periodic. The classic lid-driven cavity is the one that destabilizes earliest, the motion of the second lid having a stabilizing effect. The stabilization is maximal for α=−0.464, with smaller (negative) values tending to reduce the critical value Re^{H}. The case $\alpha=-\pi/4$, however, is a relative maximum for Re^{H}, meaning that the desymmetrisation from equal speeds has locally a slightly stabilizing effect.

The destabilization of the periodic solution occurs, for the values of the parameters prescribed here, always through a Neimark-Sacker bifurcation. The trend of the critical curve is however different from that corresponding to the Hopf bifurcation. Setting the second lid in motion has a highly destabilizing effect for the periodic solution. Therefore, the periodic solutions are confined to a very narrow range of Re for α=−0.1. A similar effect takes place for α=−0.464 despite periodic solutions being stabilized, on account of the steady solution being strongly stabilized (Fig. 9).

Quasi-periodic solutions seem to break into chaotic dynamics for all α explored. For α=−0.1 and close to $-\pi/4$, quasi-periodicity subsists within a rather narrow range of Reynolds numbers. At exactly $-\pi/4$, however, the quasi-periodic solution is strongly stabilized. It seems that the π-rotational symmetry has the effect of delaying chaos to a large extent.

Acknowledgments

This work is supported by the projects of the Northwestern Polytechnical University (No. G2021KY05103), the Natioanl Key Laboratory of Science and Technology on Aerodynamic Design and Research (No. 614220121030101), the Key Laboratory of Icing and Anti/De-icing of China Aerodynamics Research and Development Center (No. IADL20210302), the Spanish Government (Nos. FIS 2016-77849-R and PID2020-114043GB-I00), the Catalan Government (No. 2017-2017-SGR-00785), and the Barcelona Supercomputing Centre (Nos. FI-2017-2-002, FI-2017-3-0009, and FI-2016-3-0038).

Author contributions

Bo AN took in charge of the code writing, validation, and modifications. Bo AN, Weimin SANG, and Dong LI evaluated the simulation performance and prepared figures. Bo AN, Weimin SANG, Josep M. BERGADÀ, and F. MELLIBOVSKY wrote the main manuscript text. Weimin SANG, Dong LI, Josep M. BERGADÀ, and F. MELLIBOVSKY reviewed the manuscript and suggested for manuscript modifications. F. MELLIBOVSKY took the whole in charge of the present study.

Conflict of interest

Bo AN, Josep M. BERGADÀ, Weimin SANG, Dong LI, and F. MELLIBOVSKY declare that they have no conflict of interest.

References

Albensoeder S, Kuhlmann HC, 2002. Linear stability of rectangular cavity flows driven by anti-parallel motion of two facing walls. *Journal of Fluid Mechanics*, 458:153-180. https://doi.org/10.1017/S0022112002007917

Albensoeder S, Kuhlmann HC, Rath HJ, 2000. Multiple solutions in lid-driven cavity flows. I. Parallel wall motion. *Zeitschrift fuer Angewandte Mathematik und Mechanik*, 80(S3):S615-S616.

Alexakis A, Biferale L, 2018. Cascades and transitions in turbulent flows. *Physics Reports*, 767-769:1-101. https://doi.org/10.1016/j.physrep.2018.08.001

An B, Bergada JM, Mellibovsky F, 2019. The lid-driven right-angled isosceles triangular cavity flow. *Journal of Fluid Mechanics*, 875:476-519. https://doi.org/10.1017/jfm.2019.512

An B, Bergadà JM, Mellibovsky F, et al., 2020a. New applications of numerical simulation based on lattice Boltzmann method at high Reynolds numbers. *Computers & Mathematics with Applications*, 79(6):1718-1741. https://doi.org/10.1016/j.camwa.2019.10.002

An B, Mellibovsky F, Bergadà JM, et al., 2020b. Towards a better understanding of wall-driven square cavity flows using the lattice Boltzmann method. *Applied Mathematical Modelling*, 82:469-486. https://doi.org/10.1016/j.apm.2020.01.057

Auteri F, Parolini N, Quartapelle L, 2002. Numerical investigation on the stability of singular driven cavity flow. *Journal of Computational Physics*, 183(1):1-25. https://doi.org/10.1006/jcph.2002.7145

Boppana VBL, Gajjar JSB, 2010. Global flow instability in a lid-driven cavity. *International Journal for Numerical Methods in Fluids*, 62(8):827-853. https://doi.org/10.1002/fld.2040

Franjione JG, Leong CW, Ottino JM, 1989. Symmetries within chaos: a route to effective mixing. *Physics of Fluids A-Fluid Dynamics*, 1(11):1772-1783. https://doi.org/10.1063/1.857504

Guo ZL, Shi BC, Wang NC, 2000. Lattice BGK model for incompressible Navier-Stokes equation. *Journal of Computational Physics*, 165(1):288-306. https://doi.org/10.1006/jcph.2000.6616

Guo ZL, Zheng CG, Shi BC, 2002. Non-equilibrium extrapolation method for velocity and pressure boundary conditions in the lattice Boltzmann method. *Chinese Physics*, 11(4):366-374. https://doi.org/10.1088/1009-1963/11/4/310

Hammami F, Ben-Cheikh N, Ben-Beya B, et al., 2018. Combined effects of the velocity and the aspect ratios on the bifurcation phenomena in a two-sided lid-driven cavity flow. *International Journal of Numerical Methods for Heat & Fluid Flow*, 28(4):943-962. https://doi.org/10.1108/HFF-09-2016-0361

Iwatsu R, Ishii K, Kawamura T, et al., 1989. Numerical simulation of three-dimensional flow structure in a driven cavity. *Fluid Dynamics Research*, 5(3):173-189. https://doi.org/10.1016/0169-5983(89)90020-8

Jiménez J, 2012. Cascades in wall-bounded turbulence. *Annual Review of Fluid Mechanics*, 44:27-45. https://doi.org/10.1146/annurev-fluid-120710-101039

Kalita JC, Gogoi BB, 2016. A biharmonic approach for the global stability analysis of 2D incompressible viscous flows. *Applied Mathematical Modelling*, 40(15-16):6831-6849. https://doi.org/10.1016/j.apm.2016.02.033

Lemée T, Kasperski G, Labrosse G, et al., 2015. Multiple stable solutions in the 2D symmetrical two-sided square lid-driven cavity. *Computers & Fluids*, 119:204-212. https://doi.org/10.1016/j.compfluid.2015.05.022

Leong CW, Ottino JM, 1989. Experiments on mixing due to chaotic advection in a cavity. *Journal of Fluid Mechanics*, 209:463-499. https://doi.org/10.1017/S0022112089003186

Newhouse S, Ruelle D, Takens F, 1978. Occurrence of strange Axiom$A$ attractors near quasi periodic flows on T^m, $m\geqq 3$. *Communications in Mathematical Physics*, 64(1):35-40. https://doi.org/10.1007/BF01940759

Non E, Pierre P, Gervais JJ, 2006. Linear stability of the three-dimensional lid-driven cavity. *Physics of Fluids*, 18(8):084103. https://doi.org/10.1063/1.2335153

Nuriev AN, Egorov AG, Zaitseva ON, 2016. Bifurcation analysis of steady-state flows in the lid-driven cavity. *Fluid Dynamics Research*, 48(6):061405. https://doi.org/10.1088/0169-5983/48/6/061405

Perumal DA, Dass AK, 2011. Multiplicity of steady solutions in two-dimensional lid-driven cavity flows by lattice Boltzmann method. *Computers & Mathematics with Applications*, 61(12):3711-3721. https://doi.org/10.1016/j.camwa.2010.03.053

Prasad C, Dass AK, 2016. Use of an HOC scheme to determine the existence of multiple steady states in the anti-parallel lid-driven flow in a two-sided square cavity. *Computers & Fluids*, 140:297-307. https://doi.org/10.1016/j.compfluid.2016.10.013

Qian YH, D'Humières D, Lallemand P, 1992. Lattice BGK models for Navier-Stokes equation. *Europhysics Letters*, 17(6):479-484. https://doi.org/10.1209/0295-5075/17/6/001

Romanò F, Albensoeder S, Kuhlmann HC, 2017. Topology of three-dimensional steady cellular flow in a two-sided anti-parallel lid-driven cavity. *Journal of Fluid Mechanics*, 826:302-334. https://doi.org/10.1017/jfm.2017.422

Romanò F, Türkbay T, Kuhlmann HC, 2020. Lagrangian chaos in steady three-dimensional lid-driven cavity flow. *Chaos*, 30(7):073121. https://doi.org/10.1063/5.0005792

Ruelle D, Takens F, 1971. On the nature of turbulence. *Communications in Mathematical Physics*, 20(3):167-192. https://doi.org/10.1007/BF01646553

Shankar PN, Deshpande MD, 2000. Fluid mechanics in the driven cavity. *Annual Review of Fluid Mechanics*, 32:93-136. https://doi.org/10.1146/annurev.fluid.32.1.93

Vassilicos JC, 2015. Dissipation in turbulent flows. *Annual Review of Fluid Mechanics*, 47:95-114. https://doi.org/10.1146/annurev-fluid-010814-014637

Yang DX, Zhang DL, 2012. Applications of the CE/SE scheme to incompressible viscous flows in two-sided lid-driven square cavities. *Chinese Physics Letters*, 29(8):084707. https://doi.org/10.1088/0256-307X/29/8/084707

Yu PX, Tian ZF, 2018. An upwind compact difference scheme for solving the streamfunction-velocity formulation of the unsteady incompressible Navier-Stokes equation. *Computers & Mathematics with Applications*, 75(9):3224-3243. https://doi.org/10.1016/j.camwa.2018.01.043

Electronic supplementary materials

Videos S1–S12, Eq. (S1)